

**BOTTOM-UP AND DIRECTED SELF-ASSEMBLY
USING THE LATTICE BOLTZMANN METHOD**

GAURAV NATH



DEPARTMENT OF MECHANICAL ENGINEERING

INDIAN INSTITUTE OF TECHNOLOGY DELHI

JANUARY 2023

© Indian Institute of Technology Delhi (IITD), New Delhi, 2023

BOTTOM-UP AND DIRECTED SELF-ASSEMBLY USING THE LATTICE BOLTZMANN METHOD

by

GAURAV NATH

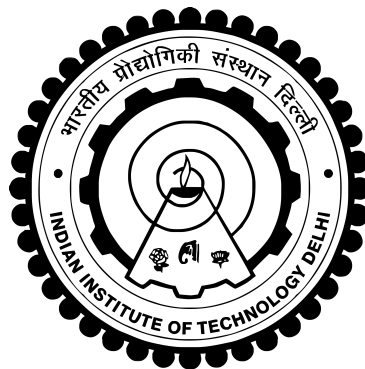
Department of Mechanical Engineering

Submitted

in fulfilment of requirements of degree of

Doctor of Philosophy

to the



INDIAN INSTITUTE OF TECHNOLOGY DELHI

JANUARY 2023

I would like to dedicate this thesis to my loving parents . . .

CERTIFICATE

This is to certify that the thesis entitled "**Bottom-up And Directed Self-assembly Using The Lattice Boltzmann Method**" being submitted by **Mr. Gaurav Nath** to the **Indian Institute of Technology Delhi** for the award of the degree of **Doctor of Philosophy** is a bonafide record of original research work carried out by him under my supervision in conformity with rules and regulations of the institute. The results presented in this thesis have not been submitted, in part or in full, to any other University or Institute for the award of any degree or diploma.



Dr. Bahni Ray

Assistant Professor

Department of Mechanical Engineering

Indian Institute of Technology Delhi

Date: 23/01/2023

ACKNOWLEDGEMENTS

I would like to express my sincere gratitude to my supervisor, Dr. Bahni Ray, for her active interest in my work, participation in all stages of problem solving and overall guidance.

I also wish to thank my research committee members, Dr. Anjan Ray, Dr. Supreet Singh Bagha and Dr. Jayati Sarkar for their valuable time and suggestions.

I appreciate the assistance given to me by my colleagues at the Computations Lab: Santosh Kushwaha, Rahul Sharma, Govind Sharma and Nitesh Kumar Sahu for always being helpful and reliable. I am grateful to Dr. Nilesh Dadasaheb Pawar for lending me the template for this thesis.

A heartfelt thanks to Rohit Mehta and Ajay Kumar Lodhi for keeping me company during my stay here, along with the rest of the 2017 Girnar PhD scholars. I am also honoured to be part of the PG music society, Udbhav, and grateful for letting me participate in their club activities.

I am forever indebted to my parents, brother, and my childhood friends for their unwavering support.



Gaurav Nath

Date: 23-1-2023

ABSTRACT

Lattice Boltzmann method (LBM) is emerging as a powerful technique in computational fluid dynamics (CFD) with applications in automotive, aerospace, energy and geoscience sectors. Based on the kinetic theory, LBM allows for better inclusion of mesoscopic physics than conventional CFD approaches. As a result, LBM has the potential to handle challenges in the field of nano and micro scale self-assembly. In this thesis, LBM is employed in two regimes: bottom-up and directed self-assembly. The scope and viability of LBM are evaluated for these applications.

In the bottom-up regime, an active interest in soft matter, the self-assembly of nanosized amphiphilic Janus spheres is attempted via LBM. Existing computational works have been done via molecular dynamics (MD) and Monte Carlo (MC) with lesser LBM representation. The present LBM studies often ignore the fluctuations in the fluid phase, essential to soft matter phenomena like Brownian motion. In this thesis, a direct numerical simulation (DNS) of amphiphilic Janus particles' self-assembly is attempted in bulk and confined arrangements. A weighted multi-relaxation time collision model is implemented to include the thermal fluctuations. Nanosized particles are treated via the momentum exchange approach combined with lubrication and close contact corrections. Features from MD, like the Janus particle interaction potential and a periodic boundary condition for particles, are also incorporated. Preliminary results of cluster size distribution, cluster properties, cluster shapes, number density and orientation profiles show some deviations from the corresponding MD studies. These are attributed to several factors namely, the difference in clustering algorithms, particle periodic boundary condition and treatment of hydrodynamic interactions between the two methods. The study affirms LBM's ability to tackle soft matter problems but with limitations, including the low computational efficiency of LBM in an inertia-free regime and the added load from incorporating fluctuations. The current LBM model could be further applied to study active and self-propelled

Janus particles.

In the directed self-assembly regime, an improved inkjet printing process is simulated via LBM. The said scheme utilizes the three-phase contact line of an evaporating drop guided by specific hydrophilic patterns for fabricating three-dimensional (3D) nanoparticle (NP) microstructures. Extensive literature is available on contact line movement, wetting on heterogeneous substrates and drop evaporation, with emphasis on the physics. These developments are incorporated in the current work to study the process parameters of a practical problem with applications in photonic and functional materials. A pseudopotential multicomponent approach is adopted for diffusion-limited evaporation of the liquid drop. NPs are one-way coupled and tracked via an advection-diffusion equation solved natively in LBM. Process parameters like pattern length, shape and surface energy difference are studied and affect the width and height of the final deposit, while different patch shapes alter the shape of the deposits closer to the hydrophilic regions. Internal flow inside the evaporating drop towards the pinned contact line regions could produce non-uniform deposits. The movement and pinning of the contact line at various points on the hydrophilic patterns are observed to produce the final shape of the deposition. Despite using a simple LBM setup, the model produces accurate results in the experimental regime of particle concentration < 1 wt%. Such simulations could help engineer novel hydrophilic patterns, saving experimental costs and effort in inkjet printing applications. Additionally, the current model could be extended to include external fields (electric and magnetic), realistic fluid properties and accurate particle depositions.

Special attention has been given to the behaviour of liquid drops on angular hydrophilic shapes. Literature on the same has been sparse in both the experimental and numerical sense. The previous methodology is adopted to study the contact line behaviour, evaporative flux distribution and evaporation rate of liquid drops on hydrophilic wedges of varying angles (30^0 to 90^0). A wedge shape is developed to isolate the effect of the wedge angle. A constraint set based on constant shape perimeter is adopted to compare the angled wedges fairly. The unpinning of the contact line is

found to occur first at the angular region of the wedges and the earliest for smaller wedge angles, for the same initial drop volume. The evaporative flux magnitude and total evaporation time did not vary significantly with the wedge angle. However, the instantaneous evaporation rate was found to be dependent on drop surface area and contact line movement. The current findings could be useful for the dynamics of particles bound on interfaces with complex curvatures and help improve inkjet printing processes where corresponding substrate patterns are employed. Drop behaviour on wedge-shaped designs could also be applied to generate subdroplets, finding applications in biological testing.

सारांश

लैटिस बोल्ट्ज़मैन मेथड (एलबीएम) ऑटोमोटिव, एयरोस्पेस, ऊर्जा और भू-विज्ञान के क्षेत्रों में एक शक्तिशाली कंप्यूटेशनल फ्लूईड डायनमिक्स (सीएफडी) की तकनीक के रूप में उभर रहा है। काइनेटिक सिद्धांत पर आधारित, एलबीएम पारंपरिक सीएफडी तकनीकों की तुलना में मेसोस्कोपिक भौतिकी को बेहतर ढंग से शामिल करने की अनुमति देता है। नतीजतन, एलबीएम में नैनो और माइक्रो स्केल सेल्फ-असेंबली के क्षेत्रों में चुनौतियों का सामना करने की क्षमता है। इस थीसिस में, एलबीएम दो क्षेत्रों में प्रयोग किया गया है: बॉटम-अप और डायरेक्टेड सेल्फ-असेंबली। इन अनुप्रयोगों के लिए एलबीएम के दायरे और व्यवहार्यता का मूल्यांकन किया जाता है।

बॉटम-अप रिजिम में एलबीएम के माध्यम से, सॉफ्ट मैटर की एक सक्रिय रुचि, नैनोसाइज्ड एम्फीफिलिक जेनस पार्टिकल की सेल्फ-असेंबली का प्रयास किया जाता है। मौजूदा कम्प्यूटेशनल कार्यों में एलबीएम का प्रतिनिधित्व कम है व ये मॉलेक्युलर डायनमिक्स (एमडी) और मोटे कार्लो (एमसी) के माध्यम से किए गए हैं। वर्तमान एलबीएम अध्ययन अक्सर थर्मल फ्लक्चुएशन्स की उपेक्षा करते हैं, जो कि ब्राउनियन मोशन जैसी सॉफ्ट मैटर प्रक्रियाओं के लिए आवश्यक है। इस थीसिस में, एम्फीफिलिक जेनस पार्टिकल की सेल्फ-असेंबली का डायरेक्ट न्यूमरिकल सिमुलेशन (डीएनएस) सीमा और सीमारहित वातावरणों में करने का प्रयास किया गया है। थर्मल फ्लक्चुएशन्स को शामिल करने के लिए एक वेटेड मल्टी-रिलैक्सेशन टाइम कोलिषन मॉडल लागू किया गया है। नैनोसाइज्ड पार्टिकल्स को लुब्रिकेशन और क्लोज कॉन्टैक्ट करेक्शन के साथ मोमेंटम एक्सचेंज अप्रोच के जरिए ट्रीट किया गया है। एमडी की विशेषताएं, जैसे जेनस पार्टिकल पोटेन्शियल और पार्टिकल सामयिक सीमा स्थिति भी शामिल हैं।

क्लस्टर आकार वितरण, क्लस्टर गुण, क्लस्टर आकार, संख्या घनत्व और अभिविन्यास प्रोफाइल के प्रारंभिक परिणाम इसी एमडी अध्ययन से कुछ विचलन दिखाते हैं। इन्हें कई कारकों का परिणाम ठहराया जाता है, जैसे कि क्लस्टरिंग एल्गोरिदम में अंतर, पार्टिकल सामयिक सीमा स्थिति और दो तरीकों के बीच हाइड्रोडायनामिक इंटरैक्शन का उपचार। यह अध्ययन एलबीएम की सॉफ्ट मैटर की समस्याओं से निपटने की क्षमता की पुष्टि करता है, लेकिन सीमाओं के साथ, जैसे जड़ता मुक्त शासन में एलबीएम की कम कम्प्यूटेशनल दक्षता और थर्मल फ्लक्चुएशन्स को शामिल करने का अतिरिक्त भार। सक्रिय और स्व-चालित जेनस पार्टिकल्स का अध्ययन करने के लिए वर्तमान एलबीएम मॉडल को आगे लागू किया जा सकता है।

निर्देशित सेल्फ-असेंबली के क्षेत्र में, एलबीएम के माध्यम से एक बेहतर इंकजेट प्रिंटिंग प्रक्रिया का अनुकरण किया जाता है। उक्त योजना तीन-आयामी (3डी) नैनोपार्टिकल (एनपी) माइक्रोस्ट्रक्चर को गढ़ने के लिए विशिष्ट हाइड्रोफिलिक पैटर्न द्वारा निर्देशित वाष्पीकरण ड्रॉप की श्री-फेज़ कॉटैक्ट लाइन का उपयोग करती है। कॉटैक्ट लाइन, सबस्ट्रेट्स वेदाबिलिटी और ड्रॉप वाष्पीकरण पर व्यापक साहित्य उपलब्ध है, जहाँ भौतिकी पर जोर दिया जाता रहा है। इन विकासों को वर्तमान कार्य में शामिल किया गया है एक व्यावहारिक समस्या के मापदंडों का अध्ययन करने के लिए, जिनका उपयोग फोटोनिक और कार्यात्मक सामग्री में किया जा सकता है। तरल ड्रॉप के डिफेयूशन-सीमित वाष्पीकरण के लिए एक स्यूडोपोटेंशियल मल्टीकंपोनेंट दृष्टिकोण अपनाया गया है। एनपी वन-वे कपलिंग के माध्यम से युक्त हैं और एलबीएम में मूल रूप से आइवेक्षण-डिफेयूशन समीकरण के माध्यम से ट्रैक किए गये हैं। पैटर्न की लंबाई, आकार और सतह ऊर्जा अंतर जैसे प्रक्रिया मापदंडों का अध्ययन किया गया है और अंतिम माइक्रोस्ट्रक्चर की चौड़ाई और ऊंचाई को प्रभावित करता है, जबकि विभिन्न पैच आकार माइक्रोस्ट्रक्चर के आकार को हाइड्रोफिलिक क्षेत्रों के करीब बदलते हैं। पिन किए गए कॉटैक्ट लाइन क्षेत्रों की ओर वाष्पित होने वाली बूंद के अंदर आंतरिक प्रवाह गैर-समान जमा उत्पन्न कर सकता है। हाइड्रोफिलिक पैटर्न के विभिन्न बिंदुओं पर कॉटैक्ट लाइन की गति और पिनिंग को अंतिम आकार का निर्माण का कारण माना जाता है। एक साधारण एलबीएम सेटअप

का उपयोग करने के बावजूद, मॉडल पार्टिकल एकाग्रता $<1 \text{ wt}\%$ के प्रायोगिक शासन में सटीक परिणाम उत्पन्न करता है। इस तरह के सिमुलेशन नए हाइड्रोफिलिक पैटर्न बनाने में मदद कर सकते हैं और इंकजेट प्रिंटिंग अनुप्रयोगों में प्रायोगिक लागत और प्रयास को बचा सकते हैं। इसके अतिरिक्त, विद्युत और चुंबकीय क्षेत्रों, यथार्थवादी द्रव गुणों और सटीक पार्टिकल माइक्रोस्ट्रक्चर को शामिल करने के लिए मौजूदा मॉडल को बढ़ाया जा सकता है।

कोणीय हाइड्रोफिलिक आकृतियों पर तरल बूंदों के व्यवहार पर विशेष ध्यान दिया गया है। इस पर साहित्य प्रयोगात्मक और संख्यात्मक दोनों अर्थों में विरल रहा है। कॉटैक्ट लाइन के व्यवहार, वाष्पशील प्रवाह वितरण और अलग-अलग कोणों के हाइड्रोफिलिक वेड्जस ($30^\circ - 90^\circ$) पर तरल बूंदों की वाष्पीकरण दर का अध्ययन करने के लिए पिछली पद्धति अपनाई गई है। कोणीय प्रभाव को अलग करने के लिए एक वेड्ज आकार विकसित किया गया है। कोणीय वेड्जस की निष्पक्ष रूप से तुलना करने के लिए समान आकार परिधि पर आधारित एक कंस्ट्रेंट सेट को अपनाया गया है। कॉटैक्ट लाइन की अनपिनिंग सबसे पहले वेड्जस के कोणीय क्षेत्र में पाई जाती है और सबसे पहले छोटे वेज एंगल्स के लिए होती है, समान ड्रॉप वॉल्यूम के लिए। वाष्पीकरणीय प्रवाह परिमाण और कुल वाष्पीकरण समय वेड्ज के कोण के साथ महत्वपूर्ण रूप से प्रभावित नहीं होता। हालाँकि, तात्कालिक वाष्पीकरण दर ड्रॉप सतह क्षेत्र और कॉटैक्ट लाइन की गति पर निर्भर पाई गई। वर्तमान निष्कर्ष जटिल वक्रता वाले इंटरफेस पर बंधे पार्टिकल्स की गतिशीलता के लिए उपयोगी हो सकते हैं और इंकजेट प्रिंटिंग प्रक्रियाओं को बेहतर बनाने में मदद कर सकते हैं जहां संबंधित सबस्ट्रेट पैटर्न कार्यरत हैं। उप-बूंदों को उत्पन्न करने के लिए वेड्ज के आकार के डिजाइनों का उपयोग किया जा सकता है जिससे जैविक परीक्षण में अनुप्रयोगों की खोज की जा सकती है।

CONTENTS

CERTIFICATE	i
ACKNOWLEDGEMENTS	ii
ABSTRACT	iii
ABSTRACT (in Hindi)	vi
CONTENTS	ix
LIST OF FIGURES	xiii
LIST OF TABLES	xxi
1 Introduction	1
1.1 Bottom-up self-assembly	1
1.1.1 Janus particle (JP) self-assembly	3
1.2 Directed self-assembly	4
1.2.1 Improved inkjet printing processes	7
1.3 Simulation methods	9
1.3.1 Importance of mesoscale methods	10
1.3.2 Lattice Boltzmann method	10
1.3.3 Why LBM?	12
1.4 Purpose of the thesis	14
1.5 Outline of the thesis	15
2 Literature Review	17
2.1 JP self-assembly simulations	17
2.1.1 LBM simulations	21
2.1.2 Trends in literature	24

2.2	Simulations on microstructure formation via drop evaporation	25
2.2.1	LBM simulations	30
2.2.2	Trends in literature	33
2.3	Gaps	35
3	Project Description	37
3.1	Aim	37
3.2	Objectives	37
3.3	Methodology and scope	37
4	Self-Assembly of Amphiphilic Janus Spheres	40
4.1	Methodology	41
4.1.1	Weighted multi-relaxation time model	41
4.1.2	Thermal fluctuations	42
4.1.3	Ladd's particle model	43
4.1.4	Boundary conditions (BC)	45
4.1.5	Lubrication correction and close contact treatment	47
4.1.6	Amphiphilic Janus potential	48
4.1.7	Simulation setup	49
4.2	Code validation	53
4.2.1	3D particle settling in a channel	53
4.2.2	Equipartition benchmark	57
4.2.3	Lubrication correction benchmark	58
4.3	Results and discussion	59
4.3.1	Janus sphere self-assembly in bulk	59
4.3.2	Janus sphere cluster properties	61
4.3.3	Cluster shapes	63
4.3.4	Janus spheres in confinement	63
4.3.5	Discussion	67
4.4	Conclusion	69

5	Microstructure Formation from Evaporating Droplets on Hydrophilic Patterns	72
5.1	Methodology	74
5.1.1	Shan-Chen multicomponent model	74
5.1.2	Diffusion-limited evaporation model	75
5.1.3	Wetting boundary condition	76
5.1.4	Advection-diffusion equation for particle phase	77
5.1.5	Simulation setup	78
5.1.6	Model overview	79
5.2	Code validation	80
5.2.1	Diffusion-limited evaporation benchmark	80
5.2.2	Grid independence study	82
5.3	Results and discussion	87
5.3.1	3P pattern contact line dynamics	87
5.3.2	3P pattern particle Peclet number variation	90
5.3.3	3P pattern surface energy variation	93
5.3.4	3P pattern length variation	95
5.3.5	Four patch (4P) pattern with patch shape variation	95
5.4	Conclusion	99
6	Drop Evaporation on Angular Hydrophilic Patterns	101
6.1	Methodology	102
6.1.1	Angular patch design	102
6.1.2	Constraint cases	103
6.1.3	Simulation setup	106
6.1.4	GPU acceleration	107
6.2	Results and discussion	110
6.2.1	Unpinning behaviour	110
6.2.2	Evaporative flux	116
6.2.3	Evaporation rate	123
6.3	Conclusion	128

7 Conclusion	130
References	137
Appendix A	163
A.1 D3Q19 lattice parameters	163
A.2 Weighted MRT D3Q19 model parameters	163
A.3 Inlet and outlet BC for D3Q19 lattice	166
A.3.1 Velocity inlet BC for fluid flow in positive x-direction	166
A.3.2 Pressure outlet BC for fluid flow in positive x-direction	168
A.4 2D view of particle going down a channel	169
A.5 GPU conversion of LBM code: PHASE 1	170
A.6 Licenses and permissions	173
List of Publications	174
Biodata of the Author	175

LIST OF FIGURES

1.1	Various parameters that can be controlled for self-assembly of JPs. . . .	2
1.2	Different categories of JPs: spherical, cylindrical, disc shaped, dumbbell shaped and vesicles/capsules.	4
1.3	Number of publications involving Janus particles from the year 2001 to present. Certain data included herein are derived from Clarivate Web of Science.© Copyright Clarivate 2021. All rights reserved.	5
1.4	Mechanisms for direct assembly of spherical NPs on geometrically patterned surfaces via convective assembly (left) and capillary assembly (right).	6
1.5	Scheme for direct assembly of gold ellipsoidal NPs into a lithographically modified substrate with traps. Inset: SEM (scanning electron microscope) micrograph of deposited ellipsoidal NPs.	7
1.6	(a) Inkjet printing scheme for 3D NP deposition. (b) SEM images (side and top view) of the different shapes of 3D controllable morphologies, scale bar - $20\mu m$	8
1.7	Classification of simulation techniques on the basis of problem length scales.	9
1.8	Schematic for streaming of populations in LBM.	12
1.9	Number of publications made in LBM from the year 2000 to present. Certain data included herein are derived from Clarivate Web of Science © Copyright Clarivate 2021. All rights reserved.	13
1.10	Treemap of the various disciplines where LBM is employed. Size of the blocks is roughly proportional to the popularity among other LBM application fields. Certain data included herein are derived from Clarivate Web of Science © Copyright Clarivate 2021. All rights reserved. . .	16

2.1	Model amphiphilic JP assembly in a slit-pore (left) and top view of one bilayer (right), determined by MD simulation.	18
2.2	Worm-like self-assembled structures in experiments (left) and MC simulation (right) of amphiphilic JPs formed on increasing the salt concentration.	19
2.3	JP self-assembled structures predicted by DPD simulation in hydrophobic (left) and hydrophilic (right) nanotubes. Uniformly coloured JPs in hydrophobic nanotube (centre).	20
2.4	Janus SCs assemblies predicted by MD-MPCD simulation for different particle aspect ratio λ and volume fraction ϕ	21
2.5	Arrangements of magnetic JPs at the interface of a hemispherical droplet predicted by LBM simulation under the influence of an applied magnetic field \mathbf{H} in varying directions.	22
2.6	Assemblies of ellipsoidal JPs under different magnetic fields $\bar{\mathbf{B}}$ predicted by LBM simulation for higher surface fraction.	23
2.7	Evaporating salt water deposits on a heated substrate in the presence of an applied alternating current (AC) and direct current (DC) predicted by MD simulation.	26
2.8	NP deposit left behind from liquid evaporating on a flat hydrophobic strip (left) and a stepped strip (right) across a hydrophilic substrate predicted by MC simulation.	27
2.9	Experimental coffee-ring stains found for spherical and non-spherical pinned drops on evaporation (top). Particle deposition profile (bottom left) and flow field (bottom right) predicted by FEM simulation.	28
2.10	Self-assembled structure of submicroparticles deposited by inkjet printing seen via atomic force microscopy (left) compared with the deposition profiles obtained from the hybrid DPD approach (right).	29

2.11	Preferential wetting affecting the final deposit during the evaporation of a colloidal drop from a heterogeneous substrate consisting of hydrophilic and hydrophobic regions, predicted by LBM simulation.	31
2.12	LBM-BD simulation of a drop pinned in a triangular shape evaporating with adsorbed NPs leading to a dried deposit.	32
4.1	(a) Particle tracking in Ladd's model and (b) halfway bounceback from a boundary node.	44
4.2	(a) Accessible and inaccessible nodes when a particle crosses a domain boundary. Schematic of the periodic boundary condition for a particle crossing the domain boundary through (b) a face, (c) an edge and (d) a corner of a cubic domain.	47
4.3	Total pair potential ϕ (normalized by $k_B T$) for different configurations (neutral, favourable and unfavourable) with $T^* = 0.167$ and $\Lambda = 3/\sigma$	49
4.4	Isometric view of the domain for the (a) bulk case and (b) confined case. yz faces (dark coloured planes) represent no-slip walls.	51
4.5	Leapfrog scheme.	52
4.6	Domain used for the particle settling in a channel benchmark.	54
4.7	x -direction particle velocity u_{px} at different timesteps for (a) case 1 ($a = 2.5$) and (b) case 2 ($a = 3.75$) of particle settling in a channel benchmark.	55
4.8	Particle trajectories for the two cases $a = 2.5, Re_p = 1$ and $a = 3.75, Re_p = 2.22$ compared against the results of Liu for the cases $a = 2.5, Re_p = 1.05$ and $a = 3.75, Re_p = 2.24$, for a particle settling in channel benchmark.	56
4.9	Time history of mean squares of the (a) translational and (b) angular velocity of particles normalized by $(3k_B T/M_p)$ and $(3k_B T/I_p)$ respectively, in the equipartition benchmark.	57
4.10	Normal lubrication force F (non-dimesionalized by $2\rho v u_p^{rel} a$) between two spheres calculated analytically (solid line) and computationally (hollow circles) as a function of surface gap h (or non-dimensional h/a).	59

4.11	Isometric view of the domain for the bulk case at equilibrium. Particle periodic images are visible here.	60
4.12	Bulk cluster size distribution at $t^* = 19.62$. (Inset) cluster size distribution from a similar MD study.	60
4.13	Plot of (a) mean cluster size N_c^{mean} vs t^* and (b) Φ vs t^* for the bulk case.	62
4.14	Variation of the average potential, kinetic and total energy per particle (normalized by $k_B T$) with time t^* for (a) the bulk case and (b) the confined case.	62
4.15	(a),(b) and (c) Comparison of cluster shapes between LBM (white background) and MD results (black background).(d) Additional cluster shapes in LBM results.	64
4.16	Comparison between LBM and MD results for (a) normalized number density profile $n^*(x)$ (b) order parameter function profile $\psi(x)$, for confined case. Equilibrium view of the confined case for (c) LBM result and (d) MD result.	65
4.17	Clusters close to the wall, viewed perpendicularly. The dark coloured plane represents the wall and the domain boundaries. Particle periodic images are shown here.	67
5.1	(a) Inkjet printing scheme for 3D NP deposition. (b) SEM images (side and top view) of the different shapes of 3D controllable morphologies, scale bar - $20\mu m$	73
5.2	Simulation domain with a grid size of $100 \times 100 \times 50$	79
5.3	(a) Contact angle θ vs. normalized time t^* for evaporating droplet, results from LBM model and CCR diffusion model. Variation of (b) normalized contact radius $R_c(t)/R_0$ and (c) normalized droplet volume $V(t)/V_0$ with normalized time t^*	81

5.4	Variation of (a) contact angle θ , (b) normalized contact diameter $D_c(t)/D_0$ and (c) normalized droplet volume $V(t)/V_0$ with time normalized by total evaporation time (t/t_e) for evaporating droplet, results from LBM model and experimental results from the no magnet case in Shyam et al.	83
5.5	Three patch (3P) pattern. Hydrophilic patches (green colored) on hydrophobic substrate (blue colored).	83
5.6	Normalized drop height H/H_0 , volume V/V_0 and pinned contact radius R/R_0 vs non-dimensional time t^* for the coarse, finer and the finest grids.	85
5.7	Sliced view of the liquid drop profiles (a) next to the substrate at $Z = 1$ (top $X - Y$ view) and (b) across the pattern at $X = N_x/2$ (side $Y - Z$ view) for all the three grids compared at the time of unpinning.	86
5.8	3P pattern droplet profile at various stages of evaporation ($t^* = 0 - 1.17$) (a) top ($X - Y$) view (slice taken at $Z = 1$), (b) side ($Y - Z$) view (slice taken at $X = N_x/2$).	88
5.9	(a) Formation of a single micro-colloidal crystal for 3P pattern, scale bar - $10\mu m$. (b) Influence of surface tension and particle concentration on deposition morphology.	89
5.10	Flow field inside the evaporating droplet on 3P pattern at $t^* = 1$. Velocity magnitude in lattice units.	90
5.11	Particle concentration ρ_c profile along the pattern (along Y -axis at $X = N_x/2$) for $Pe_c = 0.88, 1.14$ and 1.6	91
5.12	3D particle deposition morphology for $Pe_c = 0.88$ and 1.6	91
5.13	Fluid flow streamlines near the hydrophilic patch for $Pe_c = 1.6$ case, plotted over contour of particle concentration ρ_c	92
5.14	3P pattern deposition profile for varying $\theta_{R2} = 102.61^0, 124.75^0$ and 147.49^0 (a) top ($X - Y$) view (slice taken at $Z = 1$), (b) side ($Y - Z$) view (slice taken at $X = N_x/2$).	94

5.15	3P pattern deposition profile for varying $L_0 = 40, 45$ and $50 lu$ (a) top ($X - Y$) view (slice taken at $Z = 1$), (b) side ($Y - Z$) view (slice taken at $X = N_x/2$).	96
5.16	(a) 4P pattern template. Droplet (dotted line) and deposition (solid line) profiles for the 4P pattern (top view $X - Y$, slice at $Z = 1$) with (b) circular patch, (c) square patch and (d) rhombus patch. Insets: SEM images of deposition morphology for quadrilateral pattern with (b) circular patch, (c) patch with 90° interior angle, and (d) patch with 120° interior angle. Scale bar - (b) $20 \mu m$, (c) and (d) - $10 \mu m$	98
6.1	Angular hydrophilic patch schematic diagram.	102
6.2	Perimeter ratio for the $\theta_{ang} = 30^\circ$ wedge for different r_2/r_1	103
6.3	The discretized wedge patterns for $\theta_{ang} =$ (a) 30° , (b) 45° , (c) 60° , (d) 75° and (e) 90° , discretized on a 201×241 lattice. Hydrophilic regions are highlighted in red and hydrophobic regions in gray.	105
6.4	Schematic of array of structure (AoS) and structure of array (SoA) data layout schemes.	109
6.5	LBM code speedup comparison for the diffusion-limited evaporation benchmark (Section 5.2.1) run on different devices (GPUs and CPUs) for two grid sizes - $100 \times 100 \times 50$ and $200 \times 200 \times 100$	109
6.6	Drop profiles at various stages of evaporation t^* for $\theta_{ang} = 30^\circ$ wedge, (a) side ($Y - Z$) view (slice taken at $X = N_x/2$), (b) top ($X - Y$) view (slice taken at $Z = 1$) and (c) 3D view of the drop at $t^* = 0$	113
6.7	Drop profiles at various stages of evaporation t^* for $\theta_{ang} = 60^\circ$ wedge, (a) side ($Y - Z$) view (slice taken at $X = N_x/2$) and (b) top ($X - Y$) view (slice taken at $Z = 1$).	114
6.8	Drop profiles at various stages of evaporation t^* for $\theta_{ang} = 90^\circ$ wedge, (a) side ($Y - Z$) view (slice taken at $X = N_x/2$) and (b) top ($X - Y$) view (slice taken at $Z = 1$).	115

6.9	Normalized drop parameters (V/V_0 and t/t_e) at apex and base unpinning, for $\theta_{ang} = 30^0, 45^0, 60^0, 75^0$ and 90^0 wedges.	116
6.10	Evaporation flux magnitude (lattice units) contour at $t^* = 0.05$ for $\theta_{ang} = 30^0$ wedge, (a) along the drop surface ($Y - Z$ view, slice taken at $X = N_x/2$), and (b) along the contact line ($X - Y$ view, slice taken at $Z = 1$).	118
6.11	Evaporative flux magnitude (lattice units) at various stages of evaporation t^* for $\theta_{ang} = 30^0$ wedge, (a) along drop surface (along Y -axis at $X = N_x/2$), and (b) along one half of the contact line (along Y -axis and symmetric about $X = N_x/2$).	120
6.12	Evaporative flux magnitude (lattice units) at various stages of evaporation t^* for $\theta_{ang} = 60^0$ wedge, (a) along drop surface (along Y -axis at $X = N_x/2$), and (b) along one half of the contact line (along Y -axis and symmetric about $X = N_x/2$).	121
6.13	Evaporative flux magnitude (lattice units) at various stages of evaporation t^* for $\theta_{ang} = 90^0$ wedge, (a) along drop surface (along Y -axis at $X = N_x/2$), and (b) along one half of the contact line (along Y -axis and symmetric about $X = N_x/2$).	122
6.14	Variation of normalized volume V/V_0 with normalized time t/t_e for $\theta_{ang} = 30^0, 45^0, 60^0, 75^0$ and 90^0 wedges.	124
6.15	Variation of instantaneous volume removal rate (in lattice units) for $\theta_{ang} = 30^0, 45^0, 60^0, 75^0$ and 90^0 wedges with normalized time t/t_e	125
6.16	Drop surface area A_s for $\theta_{ang} = 30^0, 45^0, 60^0, 75^0$ and 90^0 wedges normalized by the initial surface area of $\theta_{ang} = 30^0$ vs normalized time t/t_e	126
6.17	Isometric view of the drop evaporating from $\theta_{ang} = 30^0$ wedge at different instants of time t^*	127
A.1	D3Q19 lattice used in this thesis.	163

A.2 2D view of the particle going down the channel for case 1 ($a = 2.5, Re_p = 1$). 169

LIST OF TABLES

4.1	Scaled parameters in LBM from physical units.	50
4.2	Parameters used for the sphere settling in a channel benchmark, all units in lattice units.	53
4.3	Comparison between the computational (u_{px}) and theoretical ($u_p^{confined}$) particle terminal velocities, all units in lattice units.	56
4.4	Comparison of cluster properties between the LBM and MD results. . .	61
4.5	Advantages and disadvantages of LBM with respect to soft matter . . .	71
5.1	Component θ values for specifying the final mixture contact angle. . . .	77
5.2	3P pattern dimensions for various grids (lattice units).	82
6.1	Parameters for the angled wedges used in the current study discretized on a 201×241 lattice, all units in lattice units.	104
6.2	Component θ values for specifying the final mixture contact angle for the wedge cases.	106
6.3	Initial contact angles at different locations on the pinned contact line for $\theta_{ang} = 30^0, 45^0, 60^0, 75^0$ and 90^0 wedges, all angles in degrees.	111
6.4	Contact angles at different locations, normalized volume (V/V_0) and normalized time (t/t_e) at first instance of unpinning (at apex) for $\theta_{ang} = 30^0, 45^0, 60^0, 75^0$ and 90^0 wedges, all angles in degrees.	111
6.5	Unpin time t/t_e and remaining drop volume V/V_0 at the instance of base unpinning for $\theta_{ang} = 30^0, 45^0, 60^0, 75^0$ and 90^0 wedges.	112
A.1	D3Q19 lattice parameters.	163
A.2	Basis vectors and normalizing factors for D3Q19 lattice.	164